End-capping hollow-core fibers with suppressed coupling into higher-order modes

Ailing Zhong[1,*], Meng Ding[2], Stanislav Zvánovec[1], Francesco Poletti[2], Matěj Komanec[1] and Radan Slavík[2]

[1]*Department of Electromagnetic Field, Czech Technical University in Prague, Technicka 1902/2, 166 27 Prague 6, Czech Republic*
[2]*Optoelectronics Research Centre, University of Southampton, Southampton, SO17 1BJ, UK*
[*]*zhongail@fel.cvut.cz*

Abstract: We propose a HCF-based component with the capability of suppressing HOMs. This component consists of a segment of SMF (working as a filter fiber to mitigate HOMs) which is fusion spliced with a section of GRIN fiber (working as a mode-field adaptor). We present the component design and illustrate 4 different situations where this component can be applied based on customized requirements/applications. The proof-of-concept experiment has been carried out to quantitatively and qualitatively characterize its HOM suppression ability. The results demonstrate that this component can suppress LP_{11} mode by 4.5 dB and 14 dB when the angle misalignment is 0° and 1.1°, respectively. In practical systems, angle misalignment is a common issue with HCF coupling which is based on free-space optics, this mode-cleaning component provides an approach to effectively and conveniently achieve modal discrimination, as well as offering a sealed compact and alignment-free HCF-based fiberized link with low connection loss. Furthermore, we glued the component with the HCF to realize HCF end-capping, which prevents occurrence of contamination on the HCF end-facet and enables stable operation without the need to cleave the end-facet.

1. Introduction

Hollow-core optical fibers (HCFs) have many unique properties such as broad and adjustable transmission windows [1], high damage threshold [2], low non-linearity in combination with low chromatic dispersion [3,4], exceptional polarization purity [5], etc. These properties are of interest in a broad range of applications, for example, optical communications [6], high-power laser delivery [7], Raman spectroscopy in gas-filled HCFs [8], or fiber-based gas lasers [9].

In many currently-studied applications such as high-power laser delivery [7] or gas-filled HCF lasers [9], light is often coupled into the HCFs from a free-space beam. This generally requires a hermetic seal of the HCF end-faces to maintain the gas composition inside and to prevent HCF end-face degradation with time [10]. Additionally, unwanted cross-coupling into HCF's higher-order modes (HOMs) often needs to be controlled. This is because excited HOMs can cause multi-path interference, which causes effects such as time-dependent output beam deformation, undesired in applications such as material processing with the laser beam.

Today, gas composition inside the HCF is typically controlled using small gas chambers at the input and output with a window enabling in and out-coupling of the light from it via a free-space beam. Such solution is also commercially available, e.g., from GLOphotonics, France. An alternative is end-capping HCF to avoid contaminants entering its microstructure and to protect it from dust or debris [11]. The first all-fiber based gas cavity was demonstrated in 2021, by splicing silica end-caps on both sides of an antiresonant HCF to achieve stable transmission efficiency and heat treatment during high-power laser delivery [9]. In these configurations, unwanted cross-coupling into/from HCF's HOMs is challenging, requiring good control of the input beam size and shape and also perfect alignment of the beam in respect to the HCF, ideally

in all 5 degrees of freedom (x,y,z, pitch, and yaw). These requirements would be strongly relaxed when using an end-cap with mode-cleaning capabilities.

In this paper, we propose an HCF end-cap with reduced unwanted cross-coupling into/from HOMs. Additionally, it can be customized to accommodate a range of input/output beam mode-field diameters (MFDs). It contains a short segment of a single-mode fiber (SMF) as a mode filter which is fusion spliced with two graded index (GRIN) multimode fibers on both input and output sides for MFD adaptation. The GRIN length can be flexibly tailored to be at or longer than 1/4 pitch length [12] to realize MFD adaptation to the used HCF and achieve low connection loss. It is anti-reflective (AR) coated on both end-facets and glued with HCF. Unlike splicing, gluing does not degrade the AR coating or the HCF end-faced microstructure and can be designed to include gas inlet/outlet [13].

In the proof-of-principle demonstration, the prepared component was 8 mm long, including 7-mm SMF and about 1-mm GRIN length in total. The component achieved insertion loss of 0.42 dB, which did not degrade when we glued it on the end-face of the HCF. We tested the suppression of the HOM coupling considering input beam perfectly-aligned (x,y,z, pitch and yaw) and also position and angle misaligned, demonstrating its mode-cleaning capabilities. For example, the input beam with angle misalignment as small as 1.1° led to LP_{11} cross-coupling as high as -13 dB (5%) when no mode-cleaning components was used. This was reduced when using our mode-cleaning end-cap by 14 dB to an acceptable level of -27 dB (0.2%). Even for a perfectly-aligned beam, the LP_{11} cross-coupling was reduced by 4.5 dB when using the mode-cleaning end-cap, most likely due to imperfect symmetry of the input beam. Such mode-cleaning end-capping solution thus significantly improves robustness of HCF systems with free-space launch, as it relaxes requirements on the input beam quality or its alignment in respect to the HCF, e.g., making x,y,z alignment acceptable in situations where full 5-axis alignment would be otherwise needed.

2. HOMs in HCFs

Modern HCFs are 'effectively single-moded', meaning they are multimoded, but engineered to have very high differential attenuation between the fundamental mode and HOMs. The lowest-attenuated HOMs (typically LP_{11} and LP_{02}) can have attenuation in 100s to 1000s of dB/km [14], making any light coupled into HOMs significantly attenuated after propagation through 10s to 100s of meters in the HCFs. However, many applications require similar or shorter lengths, e.g., laser power/pulse delivery demands often 10s of meters long. Similar or shorter lengths are used in gas sensors. Coupling into HOMs are undesired, as it causes multi-path interference at the output, distorting the beam in time, spectrum, and space. This distortion often changes in time, as it is caused by the modal interference that strongly depends on the fiber perturbations such as changing temperature or acoustic pick up [15, 16]. The multi-path interference can be strongly suppressed by reducing cross-coupling into the HOMs at the HCF input or cross-coupling from the HOMs at the HCF output or both for the best performance. Indeed, besides coupling at the HCF ends, there is also an inter-modal coupling inside the HCF, which is, however, relatively weak, e.g., -50 dB/km and -33 dB/km in two different HCFs, respectively, shown in [17].

The cross-coupling into HOMs at the HCF input is caused by mismatch of the input beam size (MFD) and shape with that of the HCF. It also increases due to any misalignment in any of the 5 degrees of freedom. At the HCF output, light propagating in the HOMs can be eliminated from the output beam, e.g., by placing a mode-cleaning component that typically re-direct the energy carried by HOMs, reducing the multi-path interference in the far field. All this is illustrated in Fig. 1, where Fig. 1(a) shows cross-coupling into HOMs at the HCF input, while Fig. 1(b) illustrates how multi-path interference between HOMs and the fundamental mode distorts the output beam. The cross-coupling into HOMs can be suppressed by employing a mode-cleaning

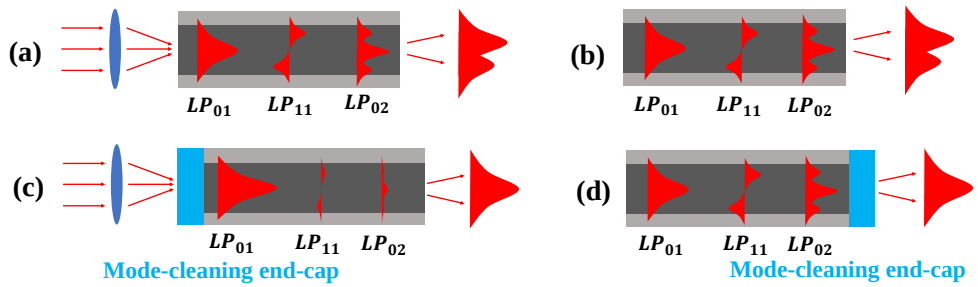

Fig. 1. (a) HOMs excitation as a consequence of imperfect launch through free-space optics. (b) Modes interfere at the HCF output, causing output beam distortions. (c) HOM cross-coupling is reduced with the mode-cleaning end-cap at the HCF input. (d) Mode-cleaning end-cap at the HCF output filters excited HOMs, making output beam symmetric and time-stable.

end-cap at the HCF input (Fig. 1 (c)). The same device at the output, Fig. 1 (d), can improve the output beam quality. Ideally, mode-cleaning end-cap can be put on both sides for the best performance.

3. Mode-cleaning end-cap: principle of operation and design

Four configurations of the proposed mode-cleaning end-cap are depicted in Fig. 2 (a - d). All four configurations contain a short segment (several mm) of SMF for mode-cleaning, fusion spliced with a GRIN fiber at the output to adapt the MFD between the SMF and the used HCF. Optionally, there can be another GRIN fiber segment spliced at the input to match the input beam MFD. A large input MFD (MFD larger than that of the HCF) can be achieved in the third configuration (Fig. 2c), which may be desired, e.g., when working with high power beams, as larger input MFD reduces the power density at the input, increasing the damage threshold, especially in the presence of dirt or dust that can be present at the input surface. A small MFD at the input can be of interest, e.g., when coupling light directly from a laser or an integrated optics chip (Fig. 2d), which typically have smaller MFD than standard single-mode fiber.

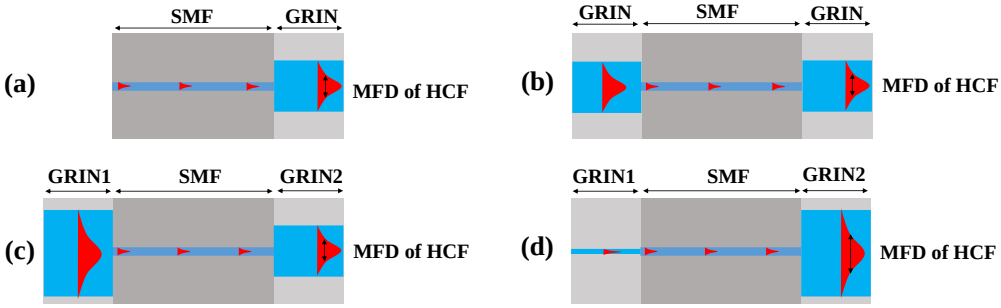

Fig. 2. Various configurations of mode-cleaning end-cap designs, all including a short segment of an SMF and one or two GRIN mode-field adapters spliced to it. (a) Output GRIN adapts MFD to that of the used HCF, (b) identical GRINs on both SMF sides for coupling of beam with MFD identical to that of the used HCF, (c) and (d) input GRINs optimized for larger (c) and smaller (d) MFD than that of the SMF, chosen according to specific requirements.

Figure. 2 (a) thus presents the simplest design with input MFD corresponding to the MFD of

the SMF. Figure. 2 (b) shows configuration with equal input and output MFDs, and Fig. 2 (c) and (d) are the most general with the input MFD larger (c) or smaller (d) than the output MFD by using different types of GRIN at the input and output.

The GRIN section that is typically 1/4 pitch long (100s of micrometers to millimeters long) works as a mode-field adapter (MFA) [18]. Its schematic representation is depicted in Fig. 3 (a). The desired mode-field size adaptation can be controlled coarsely via choice of the GRIN fiber, e.g., GRIN OM2, GRIN 100, 200, and 300 (from Berkshire Photonics, USA) provide MFD adaptation between 10 µm of SMF (here, G.657 type) to 22 µm, 31 µm, 90 µm, 116 µm, respectively when operated at 1/4 pitch [19]. Fine adjustment to accurately adapt the MFD between the SMF and the used HCF can be then achieved via fine control of the GRIN length and the GRIN-HCF gap [19], as shown in Fig. 3 (b). Thanks to sinusoidal guidance pattern of GRIN lens (one period is referred to as pitch length), the GRIN output beam converges first when the GRIN length is slightly longer than 1/4 pitch. Subsequently, it reaches a focal point (beam waist) where the beam is collimated and optimum coupling can be obtained if HCF is placed at this point and if the focal MFD matches the MFD of the HCF.

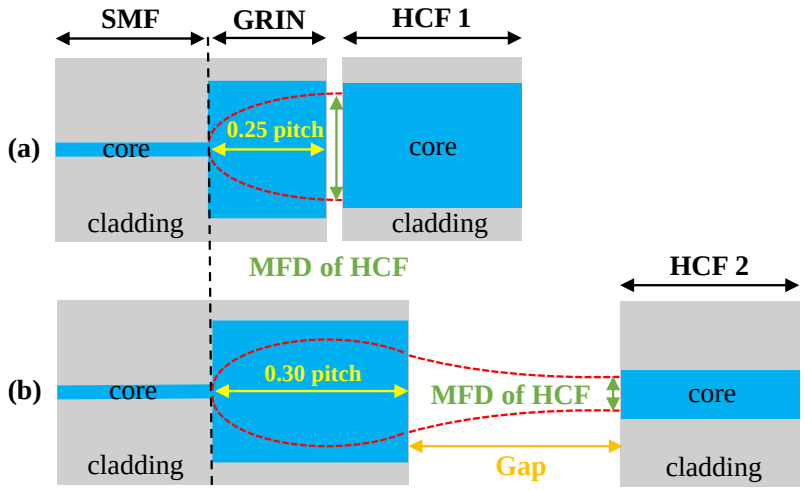

Fig. 3. Schematic representation of our mode-field adaptation design as a function of GRIN length.

4. Proof-of-concept device

In a proof-of-concept experiment, we prepared the mode-cleaning end-cap with identical GRINs on both sides (Fig. 2b). Subsequently, we characterized its performance in detail, and finally performed its permanent connection (gluing) with an HCF to demonstrate a functional end-cap.

The used HCF was 3-m long double nested antiresonant nodeless hollow-core fiber (DNANF) [20] with measured core size of 31.2 µm and its estimated fundamental mode MFD is 21.8 µm as typically the coupling into LP_{01} mode is maximized when the input beam is around 70% of the core diameter [21]. The scanning electron micrograph (SEM) of used HCF end facet is shown in Fig. 4. The loss for the fundamental mode at 1550 nm was measured to be 0.23 dB/km using cut-back method and the confinement loss of LP_{11} and LP_{02} modes was calculated [22] to be 600 dB/km and 2000 dB/km, respectively. The coupling and cross-coupling from a Gaussian mode with MFD matching that of the HCF fundamental mode was calculated to be 0.126 dB, -31.2 dB and -21.8 dB, respectively.

For GRIN, we used GRIN100 (Berkshire Photonics, USA), which based on our simulations [19] should generate MFD of 31 µm when its length is 1/4-pitch long. This is slightly larger than the MFD of the used DNANF. For better MFD adaptation, we used the method described in [19], shown in Fig. 3 (b). It uses GRIN that is slightly longer than 1/4 pitch, which makes the output beam to converge before reaching a focal point. MFD at this focal point depends on the GRIN length, enabling us to obtain desired MFD via control of the length of the used GRIN. We calculated and simulated that GRIN100 length of 465 µm (0.3 pitch) provides the desired MFD of 21.4 µm (close to the estimated MFD of the used HCF of 21.8 µm) at ~ 200 µm distance from the GRIN end facet (shown in Fig. 3b).

To prepare the mode-cleaning end-cap, we first spliced GRIN100 on both ends of a 7-mm long SMF (G.657 type) and polished the two GRINs into the desired length of 0.3 pitch. The 7-mm length of the SMF should be enough to provide the mode-cleaning, while it is short enough to avoid any undesired effect that could distort the signal due to linear and non-linear effects.

After collecting all measurement results without the mode-cleaning end-cap described below, we glued this component to the HCF using recipe described in [13]. This gluing process introduced negligible additional loss (within measurement accuracy of 0.01 dB) and provided a permanent, sealed connection.

5. Experimental setup and measurement procedures

Figure. 4 presents the experimental setup used for insertion loss and HOMs cross-coupling measurement. We elaborate on our technique to evaluate HOM coupling later. In the setup, light from a broadband source (1525 nm–1575 nm) was delivered via an SMF pigtail. It was then coupled into the HCF by virtue of 3 different means, shown in Fig. 4 (a-c), respectively. At the HCF output, light was coupled into the output SMF via a MFA and then analyzed using a power meter (PM) or optical spectrum analyzer (OSA). Reference power and spectral transmission were taken by splicing the source SMF pigtail with the output SMF.

The alignment at the HCF input and output used 5D stages (Thorlabs NanoMax MAX313D/M with pitch and yaw tilt platform APY002/M) to obtain minimum-possible coupling loss of the fundamental mode as well as to enable controlled misalignment.

The studied interface is highlighted with the green dashed boxes in Fig. 4 (b-c). To obtain a free-space, collimated input beam, we used a collimator with an aspheric lens with focal length of 18.75 mm (Thorlabs, MODEL). The collimated beam then entered into the studied interface (highlighted in green dashed box). Here, it was focused into the HCF directly (Fig. 4b) or via the mode-cleaning end-cap (Fig. 4c) using 40 mm focal length aspheric lens (Thorlabs, MODEL). This configuration imaged the 10 µm MFD of the SMF into a spot size of 40/18.75*10 µm = 21.3 µm, which is close to the MFD of the used HCF of 21.8 µm.

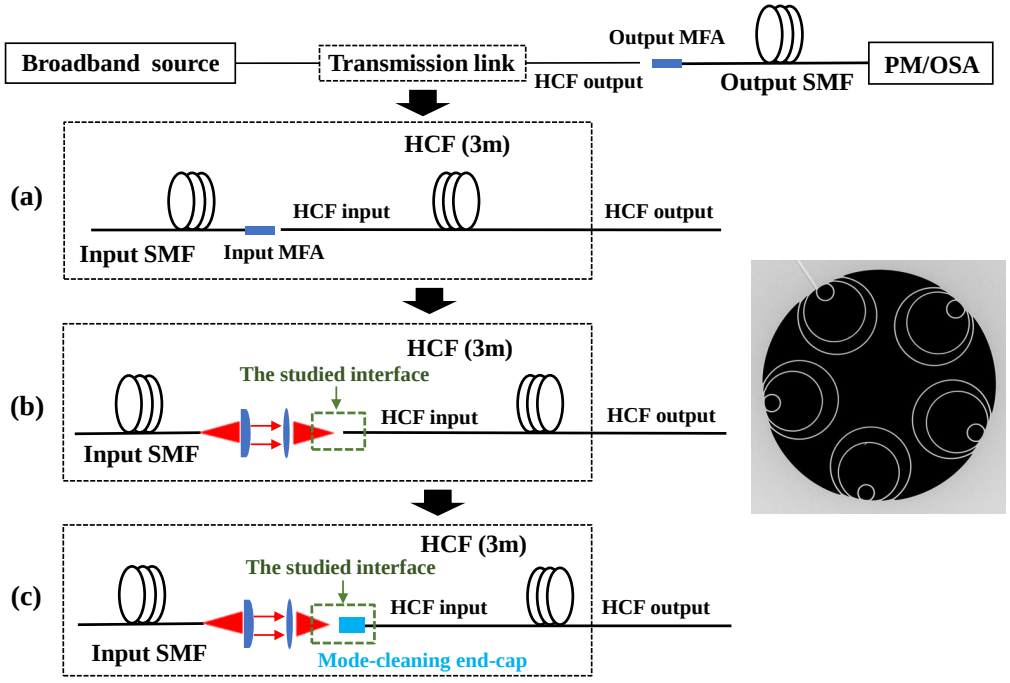

Fig. 4. Experimental setup for characterizing insertion loss and cross-coupling into HOMs. (a) Cross-coupling characterization of the used MFA by using identical MFAs at both ends, (b) characterization of HOMs cross-coupling using free-space light launch, and (c) HOMs cross-coupling characterization using free-space light launch via the mode-cleaning end-cap. Green dashed box: the studied interface. Inset: scanning electron micrograph (SEM) of used HCF.

5.1. HOM cross-coupling evaluation

In our experimental setup (Fig. 4), part of the input light is cross-coupled into HOMs at the HCF input, where they propagate with phase velocity different to that of the fundamental mode, and then cross-couple back into the output SMF, where they cause multi-path interference with the fundamental mode. This situation is represented in Fig. 5, where the upper branch represents HOM path, while the lower branch represents the fundamental mode path. The transmission characteristics are then calculated as follows.

At the HCF input, we couple light into the fundamental mode with coupling coefficient s_1 and into the HOMs with coupling coefficient c_{m1}, where m is the order of HOMs:

$$E_0(0) = E_{in}s_1,\ E_{m1}(0) = E_{in}c_{m1}, \tag{1}$$

where E_{in} is the input electric field signal, E_0 is signal coupled into the fundamental mode and E_{m1} is the signal coupled into the mth HOM. At the output of an HCF of length L, these modes accumulate different phases as they have different effective refractive indices, having electric filed of:

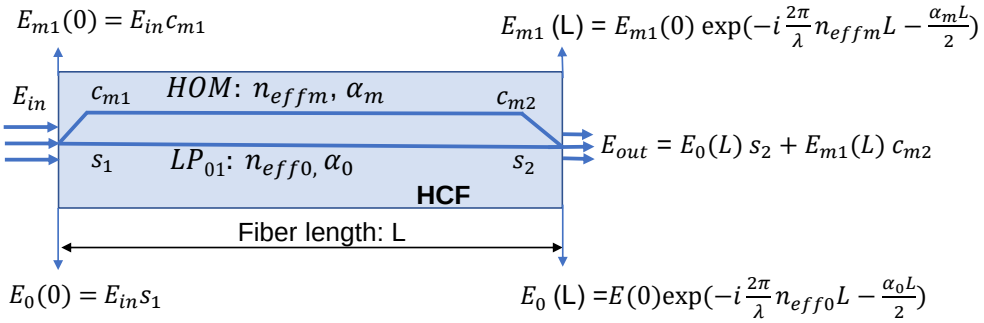

Fig. 5. Schematic representation of multi-path interference between fundamental mode and HOM in a multimoded HCF.

$$\begin{aligned} E_0(L) &= E_{in}s_1 \exp(-i\frac{2\pi}{\lambda}n_{eff0}L - \frac{\alpha_0 L}{2}), \\ E_{m1}(L) &= E_{in}c_{m1} \exp(-i\frac{2\pi}{\lambda}n_{effm}L - \frac{\alpha_m L}{2}) \end{aligned} \tag{2}$$

where n_{eff0} and n_{effm} are the effective refractive indices of the fundamental mode and mth HOM, respectively. Here, we also considered attenuation of these modes to be α_m in power ($\sqrt{\alpha_m}$ for electric field). Finally, they couple into the output with the fundamental mode coupling coefficient of s_2 and HOM cross-coupling coefficients of c_{m2}. The total (summed) field at the output is then:

$$E_{out} = E_{in}s_1s_2 \exp(-i\frac{2\pi}{\lambda}n_{eff0}L - \frac{\alpha_0 L}{2}) + \sum_{m=1}^{N} E_{in}c_{m1}c_{m2} \exp(-i\frac{2\pi}{\lambda}n_{effm}L - \frac{\alpha_m L}{2}) \tag{3}$$

The transmittance (output power divided by the input power of E_{in}^2) is:

$$\begin{aligned} T &= E_{out} \cdot E_{out}^* / E_{in} \cdot E_{in}^* \\ &\approx s_1^2 s_2^2 \exp(-\alpha_0 L) + 2\sum_{m=1}^{N} s_1 s_2 c_{m1} c_{m2} \exp\Big[\frac{-(\alpha_0 + \alpha_m)L}{2}\Big] \cos(\frac{2\pi}{\lambda}\Delta n_m L), \end{aligned} \tag{4}$$

where $\Delta n_m = n_{eff0} - n_{effm}$. The first term represents the transmission of the fundamental mode, the second term shows beating between the fundamental mode and each HOM. We do not show the last term corresponding to beating between HOMs, as it is significantly smaller than the first two terms when considering predominantly fundamental mode launch, i.e., $s_1 \gg c_{m1}$, $s_2 \gg c_{m2}$. Moreover, we can neglect the transmission loss of the fundamental mode as $\alpha_0 \ll \alpha_m$. Thus,

$$T \approx s_1^2 s_2^2 + 2\sum_{m=1}^{N} s_1 s_2 c_{m1} c_{m2} \exp\Big(\frac{-\alpha_m L}{2}\Big) \cos(\frac{2\pi}{\lambda}\Delta n_m L) \tag{5}$$

The beating between the fundamental mode and each HOM (2nd term) happens at different beating frequencies. Consequently, Fourier transform of Eq. 5 contains peaks at zero frequency (i.e., DC component, the peak amplitude represents $s_1^2 s_2^2$) and the beating frequencies (i.e., $\frac{2\pi}{\lambda}\Delta n_m L$), enabling us to isolate amplitude of the beating between the fundamental mode and each of the HOMs. Using n_{eff0} and n_{effm} obtained from simulations [18], we can then identify which peak corresponds to which HOM. As follows from Eq. 5, this beating is proportional to $s_1 s_2 c_{m1} c_{m2}$, while transmission power is proportional to $s_1^2 s_2^2$. This analysis is an extension of that presented in [18], where only symmetric situation ($c_{m1} = c_{m2}$, $s_1 = s_2$) was considered.

The above analysis shows us that we can measure product of the coupling $s_1 s_2$ and subsequently also cross-coupling coefficients $c_{m1} c_{m2}$ at both interfaces, but not directly c_{m1} and c_{m2}, which is desired to characterize a single interface, which we are interested in here. To obtain the cross-coupling coefficients at a single interface, we used the following measurement sequence.

Firstly, we used the same output MFA during all the measurements, as illustrated in Fig. 4. Subsequently, s_2 and c_{m2} stayed constant during all the characterization. To find values of s_2 and c_{m2}, we used set-up shown in Fig. 4a in which we used an identical MFA at the input side to that used at the output side, obtaining $c_{m1} = c_{m2}$, $s_1 = s_2$. The above analysis enabled us to extract $s_2^2 = s_1 s_2$ and subsequently also $c_{m2}^2 = c_{m1} c_{m2}$ and thus evaluate s_2 and c_{m2}. This required knowledge of the attenuation of the HOMs, which we mentioned earlier to be 0.23 dB/km, 600 dB/km, 2000 dB/km for the LP_{01}, LP_{11} and LP_{02} modes, respectively. Subsequently, we used free-space coupling directly into the HCF (Fig. 4b). The fundamental mode coupling s_1 and HOM cross-coupling c_{m1} were evaluated using above analysis that gave us quantities of $c_{m1} c_{m2}$ and $s_1 s_2$. As we have already evaluated s_2 and c_{m2} using setup in Fig. 4a, we were able to obtain the desired coupling s_1 and cross-coupling c_{m1}. After optimizing fundamental mode launch using all 5 degrees of freedom, we introduced controlled misalignment in the x-axis and launch angle and measured the insertion loss and HOM cross-coupling. Finally, we inserted the mode-cleaning end-cap (Fig. 4c) and repeated the measurements performed without the mode-cleaning end-cap.

5.2. Device characterization

Figure. 6 presents the measured transmission spectra for direct free-space launch (a-c) and through the mode-cleaning end-cap (d-f), including optimum angle alignment (a,d), angle misalignment by 0.55° (b,e) and 1.1° (c,f), all for optimum x,y,z alignment (blue), and misalignment in the x-axis by 2 (red), 4 (yellow), 6 (violet), and 8 µm (green).

We can see that the insertion loss increases with the misalignment of the x-axis or the angle. In the most extreme misalignment studied case (1.1° angle offset and 8 µm), it corresponds to about 3 dB degradation in respect to the perfectly-aligned case. The beating between the fundamental mode and HOMs manifest itself as spectral ripples. We see that amplitude of the spectral ripples is almost invisible for perfect alignment (both, with and without the mode-cleaning end-cap), but increases with the angle and x-axis misalignment. This increase is visibly smaller when mode-cleaning end-cap is used, e.g, the peak-to-bottom ripple amplitude for 1.1° angle misalignment and perfect x,y alignment is 0.2 dB without and 0.1 dB with the mode-cleaning end-cap, clearly showing its mode-cleaning capabilities.

To evaluate mode-cleaning capabilities quantitatively, we evaluated first c_{m2} and s_2 obtained using setup shown in Fig. 4 (a). We obtained fundamental mode coupling loss of -0.13 dB [calculated as $10\log(s_1^2)$, $s_1^2 = 0.97$], cross-coupling into LP_{11} and LP_{02} modes of -34.6 dB and -27 dB, respectively. These values are in good agreement with simulations considering the MFD produced by the MFA matches that of the used HCF. The predicted cross-coupling are -0.126 dB, -31.2 dB and -21.8 dB into the fundamental, LP_{11} and LP_{02} modes, respectively. In the next step, we extracted coupling and cross-coupling coefficients from the measured data (Fig. 6) using the above-discussed analysis.

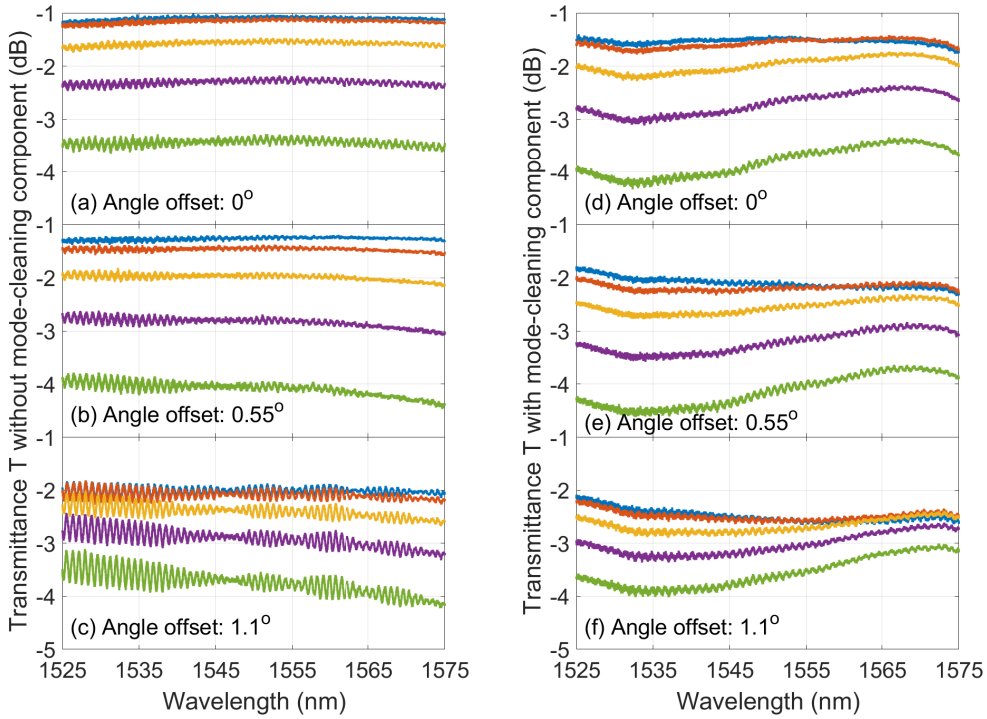

Fig. 6. Transmission spectra using direct free-space launch with angle offset of (a) 0°, (b) 0.55°, and (c) 1.1°; transmission spectra when launching through the mode-cleaning end-cap with angle offset of (d) 0°, (e) 0.55°, (f) 1.1°. The blue, red, yellow, violet, and green curves represent x-axis misalignment of 0 µm, 2 µm, 4 µm, 6 µm and 8 µm, respectively.

Figure. 7 presents the cross-coupling into LP_{11} (a, b) and LP_{02} (c, d) mode respectively, comparing the performance with and without the mode-cleaning end-cap, under angle misalignment of 0° (a, c) and 1.1° (b, d), and distance misalignment of 0 to 8 µm.

In Fig. 7 (a), we can see that under optimum alignment (0° angle and 0 µm offset), the cross-coupling into LP_{11} mode reduced from -30.5 dB to -35 dB (4.5 dB improvement) with the help of the mode-cleaning end-cap. We believe the degradation when not using the mode-cleaning end-cap is due to a slight ellipticity of the input beam, perhaps due to an imperfect telescope alignment. Such slight ellipticity is likely to happen in practice using free-space beams. Furthermore, in Fig. 7 (a), we can see that the cross-coupling into LP_{11} mode increases with distance misalignment. For example, the excitation of LP_{11} mode increased from -30.5 dB (under optimum alignment) to -20 dB (under 8 µm distance misalignment). However, the cross-coupling can be constantly suppressed by $\sim$ 4 dB assisted by the mode-cleaning end-cap.

Apart from distance misalignment, the LP_{11} mode excitation also increases with the angle misalignment, which can be seen through the comparison between Fig. 7 (a) and (b). For instance, at 1.1° angle misalignment with optimized distance alignment (0 µm offset), the cross-coupling into LP_{11} mode boosted from -30.5 dB to -13 dB. In this case, by the virtue of our mode-cleaning end-cap, the LP_{11} excitation was significantly reduced from -13 dB to -27 dB

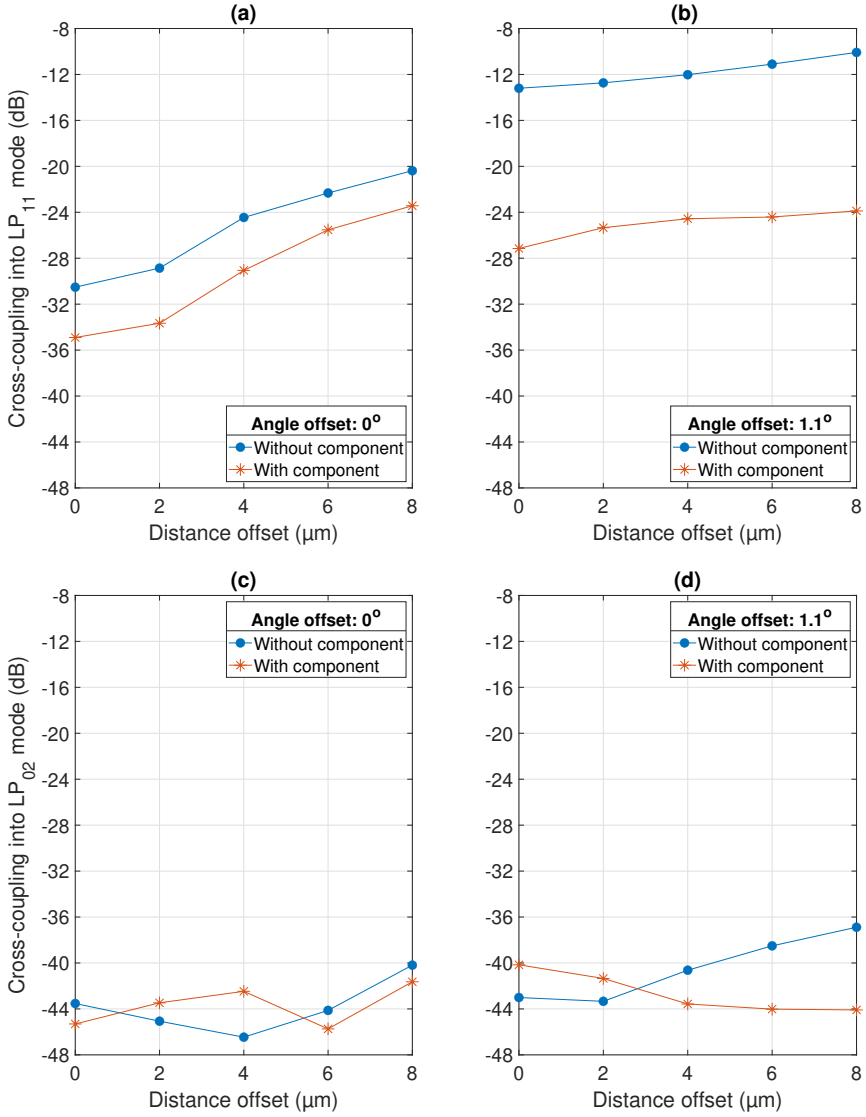

Fig. 7. Comparison of cross-coupling into LP_{11} mode with angle misalignment of (a) 0° and (b) 1.1°; cross-coupling into LP_{02} mode with angle misalignment of (c) 0° and (d) 1.1°. Blue dots: without mode-cleaning end-cap, orange dots: with mode-cleaning end-cap.

(14 dB improvement).

As for LP_{02} mode suppression (Fig. 7c and d), as the cross-coupling into LP_{02} mode is much lower than LP_{11} mode, many of the measurements are close to noise level. We can observe visible LP_{02} mode excitation only when the setup is under misalignment. For example, in Fig. 7 (d) with angle offset of 1.1°, LP_{02} mode excitation increases to -37 dB when the distance offset increases to 8 μm. However, with the help of the mode-cleaning end-cap, it effectively suppressed LP_{02} mode below -40 dB.

In practical systems with free-space optics coupling, our component will be appreciated due to its prominent capability of HOMs suppression when the angle misalignment is a common issue.

6. Conclusions

We propose a mode-cleaning component consists of a section (e.g., several millimeter long) of SMF (works as a filter fiber and is responsible for mitigating HOMs), which is fusion spliced with a short segment (e.g., hundreds of micrometer long) of GRIN fiber (serving as a mode-field adaptor). This component can be tailored to adapt various HCFs with diverse categories and dimensions. We illustrated the idea and presented 4 types of component designs based on different requirements/applications, as well as carried out proof-of-concept experiments. The results quantitatively and qualitatively demonstrated that this component successfully suppressed LP_{11} mode by 14 dB when there is only 1.1° angle misalignment. In practical systems with free-space optics coupling, angle misalignment is a common issue which can generate prominent HOMs and incur unwanted multi-path interference. In this paper, we propose an effective and convenient solution to tackle this issue, by customizing GRIN length of the component to adapt the HCF and gluing the component with the HCF. Our component makes it possible to combine the capability of suppressing HOMs and alignment-free compact HCF-based fiberized link with low-loss connection.

Acknowledgement

This work was supported by the Czech Science Foundation (GACR) grant GA22-32180S and by the EPSRC projects EP/P030181/1 and EP/W037440/1.

Disclosures

The authors declare no conflicts of interest.

References

1. B. Debord, A. Amsanpally, M. Chafer, A. Baz, M. Maurel, J.-M. Blondy, E. Hugonnot, F. Scol, L. Vincetti, F. Gérôme *et al.*, "Ultralow transmission loss in inhibited-coupling guiding hollow fibers," Optica **4**, 209–217 (2017).
2. M. Michieletto, J. K. Lyngsø, C. Jakobsen, J. Lægsgaard, O. Bang, and T. T. Alkeskjold, "Hollow-core fibers for high power pulse delivery," Opt. Express **24**, 7103–7119 (2016).
3. D. J. Richardson, N. Wheeler, Y. Chen, J. R. Hayes, S. R. Sandoghchi, G. T. Jasion, T. D. Bradley, E. N. Fokoua, Z. Liu, R. Slavík *et al.*, "Hollow core fibres and their applications," in *Optical Fiber Communication Conference,* (Optica Publishing Group, 2017), pp. Tu3H–1.
4. A. Zhong, R. Slavík, D. Dousek, D. Suslov, S. Zvánovec, F. Poletti, D. J. Richardson, and M. Komanec, "Direct and low-loss connection between a hollow-core optical fiber and a dispersion compensating fiber for dispersion-free delivery of short optical pulses in hollow-core fiber," in *High-Power Laser Materials Processing: Applications, Diagnostics, and Systems XII,* vol. 12414 (SPIE, 2023), pp. 18–22.
5. A. Taranta, E. Numkam Fokoua, S. Abokhamis Mousavi, J. Hayes, T. Bradley, G. Jasion, and F. Poletti, "Exceptional polarization purity in antiresonant hollow-core optical fibres," Nat. Photonics **14**, 504–510 (2020).
6. F. e. Poletti, N. Wheeler, M. Petrovich, N. Baddela, E. Numkam Fokoua, J. Hayes, D. Gray, Z. Li, R. Slavík, and D. Richardson, "Towards high-capacity fibre-optic communications at the speed of light in vacuum," Nat. Photonics **7**, 279–284 (2013).
7. X. Zhu, D. Wu, Y. Wang, F. Yu, Q. Li, Y. Qi, J. Knight, S. Chen, and L. Hu, "Delivery of cw laser power up to 300 watts at 1080 nm by an uncooled low-loss anti-resonant hollow-core fiber," Opt. Express **29**, 1492–1501 (2021).
8. F. Benabid, J. C. Knight, G. Antonopoulos, and P. S. J. Russell, "Stimulated Raman scattering in hydrogen-filled hollow-core photonic crystal fiber," Science **298**, 399–402 (2002).
9. J. Shi, X. Ye, Y. Cui, W. Huang, H. Li, Z. Zhou, M. Wang, Z. Chen, and Z. Wang, "All-fiber gas cavity based on anti-resonant hollow-core fibers fabricated by splicing with end caps," in *Photonics,* (MDPI, 2021), p. 371.
10. S. Rikimi, "Impact of internal pressure and gas composition on the long-term optical performance of hollow core optical fibres," Ph.D. thesis, University of Southampton (2022).
11. D. Parra, S. Yerolatsitis, J. Wahlen, D. C. Delgado, M. A. Cooper, J. E. Antonio-Lopez, A. Schülzgen, and R. A. Correa, "Antiresonant hollow core fiber endcaps for laser delivery and sensing," in *Laser Technology for Defense and Security XVIII,* (SPIE, 2023), p. PC125150D.
12. A. Zhong, D. Dousek, D. Suslov, S. Zvánovec, E. N. Fokoua, F. Poletti, D. J. Richardson, R. Slavík, and M. Komanec, "Hollow-core to standard fiber interconnection with customized air-gap distance," in *2022 Conference on Lasers and Electro-Optics (CLEO),* (IEEE, 2022), pp. 1–2.

13. D. Suslov, T. W. Kelly, S. Rikimi, A. Zhong, A. Taranta, S. Zvánovec, F. Poletti, D. J. Richardson, M. Komanec, N. Wheeler *et al.*, "Towards compact hollow-core fiber gas cells," in *2022 Conference on Lasers and Electro-Optics (CLEO),* (IEEE, 2022), pp. 1–2.
14. F. Poletti, "Nested antiresonant nodeless hollow core fiber," Opt. express **22**, 23807–23828 (2014).
15. M. N. Petrovich, F. Poletti, and D. J. Richardson, "Analysis of modal interference in photonic bandgap fibres," in *2010 12th International Conference on Transparent Optical Networks,* (IEEE, 2010), pp. 1–4.
16. A. Cubillas, M. Silva-Lopez, J. Lazaro, O. Conde, M. Petrovich, and J. Lopez-Higuera, "Methane detection at 1670-nm band using a hollow-core photonic bandgap fiber and a multiline algorithm," Opt. Express **15**, 17570–17576 (2007).
17. A. Nespola, S. Straullu, T. D. Bradley, K. Harrington, H. Sakr, G. T. Jasion, E. N. Fokoua, Y. Jung, Y. Chen, J. R. Hayes *et al.*, "Transmission of 61 c-band channels over record distance of hollow-core-fiber with l-band interferers," J. Light. Technol. **39**, 813–820 (2021).
18. D. Suslov, M. Komanec, E. R. N. Fokoua, D. Dousek, A. Zhong, S. Zvánovec, T. D. Bradley, F. Poletti, D. J. Richardson, and R. Slavík, "Low loss and high performance interconnection between standard single-mode fiber and antiresonant hollow-core fiber," Sci. Reports **11**, 1–9 (2021).
19. A. Zhong, M. Ding, D. Dousek, D. Suslov, S. Zvánovec, F. Poletti, D. J. Richardson, R. Slavík, and M. Komanec, "Gap design to enable functionalities into nested antiresonant nodeless fiber based systems," Opt. Express **31**, 15035–15044 (2023).
20. G. T. Jasion, H. Sakr, J. R. Hayes, S. R. Sandoghchi, L. Hooper, E. N. Fokoua, A. Saljoghei, H. C. Mulvad, M. Alonso, A. Taranta *et al.*, "0.174 dB/km hollow core double nested antiresonant nodeless fiber (DNANF)," in *2022 Optical Fiber Communications Conference and Exhibition (OFC),* (IEEE, 2022), pp. 1–3.
21. V. Zuba, H. C. H. Mulvad, R. Slavík, H. Sakr, F. Poletti, D. J. Richardson, and E. N. Fokoua, "Limits of coupling efficiency into hollow-core antiresonant fibres," J. Light. Technol. (2023).
22. E. N. Fokoua, S. A. Mousavi, G. T. Jasion, D. J. Richardson, and F. Poletti, "Loss in hollow-core optical fibers: mechanisms, scaling rules, and limits," Adv. Opt. Photonics **15**, 1–85 (2023).